npj | climate and atmospheric science

Article

Published in partnership with CECCR at King Abdulaziz University

https://doi.org/10.1038/s41612-025-01301-8

Reversal of the Tibetan snow-India Burma trough relationship

Chao Zhang[1,2] ✉ & Anmin Duan[1] ✉

Variations in the winter India-Burma trough (IBT) are associated with local cyclonic anomalies over the Bay of Bengal and modulated by mid-latitude teleconnections. However, spring IBT variability remains poorly understand, despite trough-base precipitation being substantially greater than in winter. Here, we identify a reversal in the spring IBT-Tibetan Plateau snow cover (TPS) relationship around the year 2000. This shift corresponds to eastward displacement of the trough-base before 2000, followed by a retreat toward the Bay of Bengal. Snow-perturbation experiments and moist potential vorticity diagnostics show that during 1979–1999, high TPS enhances atmospheric disturbances ahead of the trough and weakens them near its base. This process hence triggers an eastward displacement of the IBT. During 2000–2020, high TPS exerts largely opposite effects. Furthermore, the Pacific Decadal Oscillation (PDO) modulates this IBT-TPS linkage reversal. In the coming decades, a projected shift to a positive PDO phase is expected to promote IBT eastward displacement, enhancing spring precipitation in East Asia while increasing drought risk over the Indochina Peninsula. Our results hence provide a basis for improving seasonal projections and assessing climate risks across monsoon Asia.

Under the blocking effect of the Tibetan Plateau, the subtropical westerly splits into two branches; its southern branch forms the India-Burma (now Myanmar) trough (IBT), a semi-permanent low-pressure trough over the Bay of Bengal that typically emerges during boreal winter and spring[1–3]. Climatologically, the dominant feature of the global tropics and subtropics in spring is a system of four prominent troughs (Supplementary Fig. 1a). Among them, the spring IBT is characterized by the deepest base and southernmost position. The associated precipitation extends from East Asia across the entire North Pacific, representing the most extensive rainfall coverage of any global trough system.

The intensity and positional shifts of the IBT exert a profound influence on climate anomalies over the Asian continent and western Pacific, impacting tropical cyclones[4], large-scale precipitation[2,5], droughts[6,7], and persistent cold spells[8,9]. Specifically, the March-April IBT intensity serves as a reliable indicator for seasonal forecasting of tropical cyclones in the Western North Pacific and South China Sea[4]. A stronger IBT is correlated with above-normal temperature and precipitation in eastern East Asia but below-normal temperature and precipitation in India[5]. A weak IBT, on the other hand, is unfavorable for rainfall in Yunan (a province in China) and is a major factor behind the region's extreme drought in 2009–2010[6].

The IBT exhibits significant variability across synoptic, interannual, and interdecadal timescales[1,2,10]. The cyclonic circulation anomaly over the Bay of Bengal modulates IBT fluctuations by controlling its vorticity intensity. On synoptic timescales, the South Asian jet wave train propagates to East Asia within 4–6 days during winter[11–13], modulating this cyclone anomaly[13–15]. On interannual timescales, the deepening of the winter IBT is linked to La Niña via westerly jet waviness and tropical Kelvin waves[2,16,17], a linkage may strengthen interdecadally by a negative Pacific Decadal Oscillation (PDO) phase since 2000[17]. From the land surface, decreased Tibetan Plateau soil temperature strengthens the winter IBT by affecting upper-level westerlies[18,19]. Importantly, a strengthened winter IBT corresponds to an anomalous cyclone over the Bay of Bengal. The southerlies on its eastern flank promote rainfall in East and Southeast Asia, whereas northerlies on its western flank suppress it in South Asia, thereby establishing a direct link between IBT and Asian precipitation[2,5].

The spring IBT has received less attention than its winter counterpart, owing to the complex westerly-monsoon interaction during the seasonal transition[20,21], as well as the spring predictability barrier of El Niño-Southern Oscillation (ENSO)[22–24], which together present a challenge for isolating and predicting its dynamics. Notably, the climatological spring IBT exhibits an ~8-fold increase in trough base precipitation and a 1–2-fold downstream strengthening compared to winter (Supplementary Fig. 1d), which is attributed to a deeper trough base and a sharper downstream tilting, and a 5–7° northward shift over the western Pacific (Supplementary Fig. 1b, c). These distinctive features underscore the need to investigate the mechanisms governing spring IBT variability.

[1]Center for Marine Meteorology and Climate Change, State Key Laboratory of Marine Environmental Science, College of Ocean and Earth Sciences, Xiamen University, Xiamen, China. [2]Marine Biogeochemistry Division, GEOMAR Helmholtz Centre for Ocean Research Kiel, Kiel, Germany.
✉e-mail: chaozhang@xmu.edu.cn; amduan@xmu.edu.cn

Here, we examine the relationship between spring IBT and Tibetan Plateau thermal forcing, using TPS as the physical driver. This is motivated by three main considerations: (1) A spring TPS dipole pattern, characterized by reduced snow in the west and increased snow in the east, favors the formation of an anomalous cyclonic circulation over the Bay of Bengal[25]. Since this system is a key regulator of IBT, such a TPS pattern may establish a linkage with IBT variability. (2) The spring ENSO predictability barrier limits the forecast skill during this season[22–24]; however, persistent TPS anomalies provide a valuable source of predictability[26–29] that helps overcome this barrier. (3) Moreover, spring TPS exerts a prolonged thermal influence on the Plateau and its surroundings, and hence alters the subsequent Asian monsoon by alternating the intensity of the Plateau's thermal and hydrological forcings[21,30]. Our observational analysis reveals a regime shift in the TPS-IBT linkage around 2000. Through targeted numerical experiments and theoretical diagnostics, this study aims to quantify how TPS anomalies influence the position and strength of the spring IBT, and how this linkage has changed since 2000. Our work seeks to contribute to advance in seasonal monsoon projection and regional climate adaptation strategies.

Results

Regime shift in TPS-IBT linkage

During the extreme low-TPS year of 1996 (−1.5σ), positive precipitation anomalies emerged in the IBT downstream sector, whereas during the high-TPS year of 2011 (+1.5σ), negative precipitation anomalies occurred downstream (Supplementary Fig. 2). These contrasting responses motivate us to investigate the TPS-IBT linkage. Following previous definitions of the IBT based on 700 hPa vorticity[10,13] or geopotential height[18], we calculate both vorticity-based and height-based spring IBT indices (see "Methods"), and examine their 19-year and 21-year sliding correlations with the TPS index (Fig. 1a; the height-based IBT index × (−1)). The results show significant ($p < 0.05$) negative correlations from 1979 to 1999. However, by 2010, such sliding correlations shift to significant ($p < 0.1$) positive values (centered on 2010, i.e., spanning 2000–2020), indicating an opposite regime during 2000–2020.

Spatially, high-TPS years during 1979–1999 correspond to negative vorticity anomalies at the trough base (Fig. 1d), contrasting with the positive anomalies in 2000–2020 (Fig. 1e). This reversal marks a shift from negative to positive TPS-IBT correlation. Concurrently, high-TPS years in 1979-1999

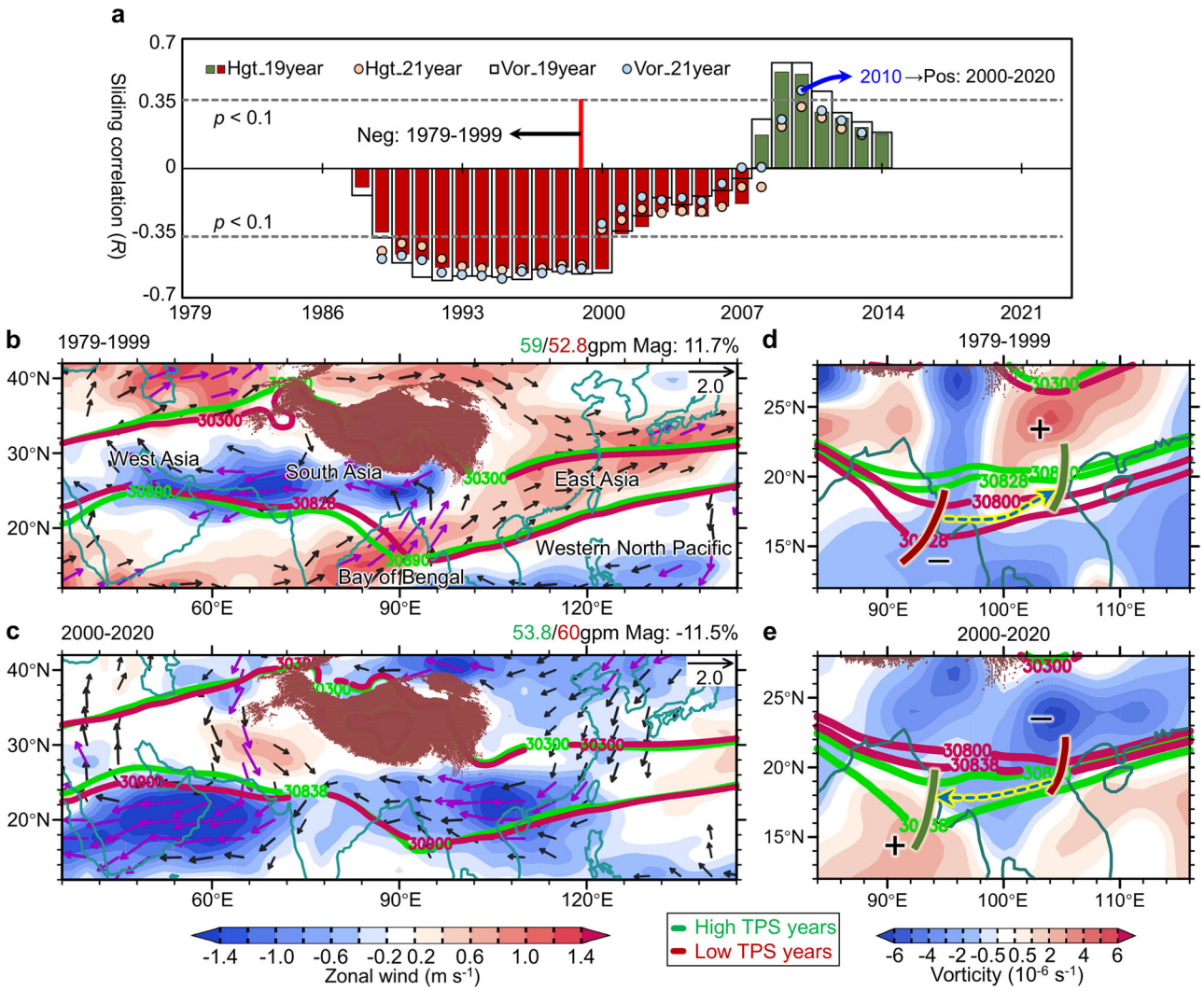

Fig. 1 | Regime shift in TPS-IBT interannual linkage. a Sliding correlation (19-/21-year window) between the spring (March-April-May) Tibetan Plateau snow cover (TPS) and the India-Burma trough (IBT) indices during 1979-2023. IBT indices derived from 700 hPa geopotential height (multiplied by -1) and vorticity fields. Horizontal dashed lines: 90% significance thresholds. **b** Spring wind (vector) and zonal wind (shading) anomalies at 700 hPa during 1979–1999, obtained by differences between high and low TPS years. Green contours (10^{-1} gpm): 700 hPa geopotential height for high-TPS years (gradient = 59 gpm). Red contours: Low TPS year conditions (gradient = 52.8 gpm). Height gradient is 11.7% larger during high TPS years. **c** As in (**b**), but for 2000–2020. Height gradients: high-TPS = 53.8 gpm, low-TPS = 60 gpm; 11.5% smaller during high-TPS years. **d**, **e** As in (**b**, **c**) but showing IBT displacement and 850 hPa vorticity (shading). Data sources: NOAA satellite snow cover and ERA5 circulation fields.

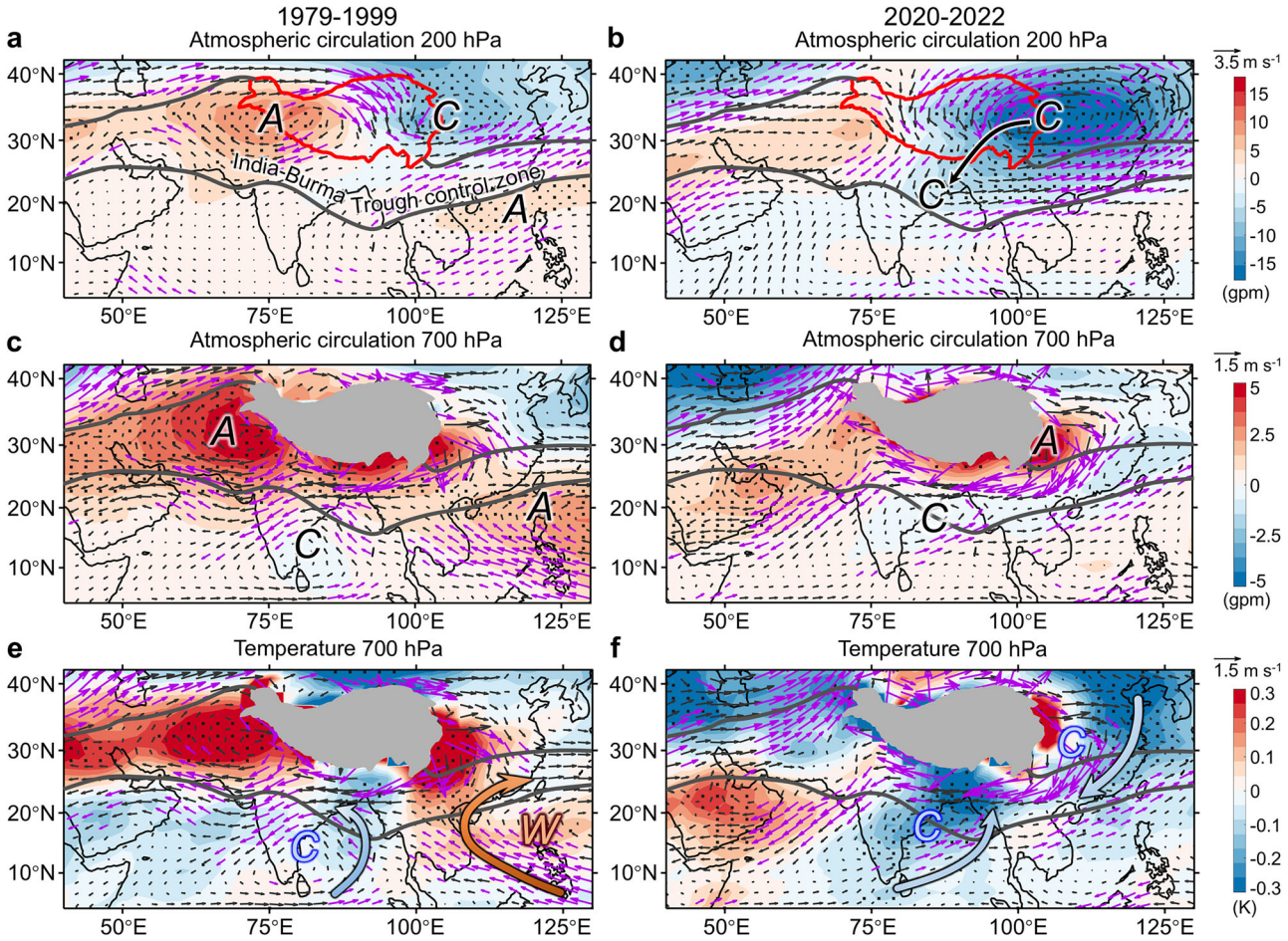

Fig. 2 | Modeled impacts of TPS forcing on IBT variations. a Spring geopotential height (shading) and wind (vector) at 200 hPa in responses to quasi-seesaw TPS forcing (1979–1999), displayed as the ensemble mean differences ($Pos^{SS}_{Exp} - Neg^{SS}_{Exp}$). **b** As in (**a**), but for coherent TPS forcing (2000–2020; $Pos^{CHR}_{Exp} - Neg^{CHR}_{Exp}$). **c**–**f** As in (**a**, **b**), but depicting 700 hPa circulation and temperature responses. All snow perturbation experiments were conducted using the CESM-LEN (see "Methods"). Black "A"/"C": Anticyclonic/cyclonic circulation. Blue "C" and red "W": cold/warm advection. Black dots and purple vectors indicate regions with statistical significance at the 95% level (two-sided *t*-test). Black contours: IBT control zone (700 hPa geopotential height climatology: 3030/3081.5 gpm). Observational counterparts are presented in Supplementary Fig. 5.

exhibit elevated geopotential height and 11.7% stronger height gradients than low-TPS years (Fig. 1b and Supplementary Fig. 3), opposing conditions in 2000–2020, which show reduced height field and 11.5% weaker gradients (Fig. 1c). The strengthened pressure gradients during 1979-1999 accelerate downstream westerlies, whereas weakened gradients post-2000 suppress them (Fig. 1b, c). These systematic reversals validate a regime shift in the TPS-IBT relationship.

As a semi-permanent low-pressure system, IBT trough base changes potentially trigger downstream responses[15]. During 1979–1999, high-TPS years are associated with negative vorticity anomalies at the trough base alongside positive downstream anomalies, favoring an eastward displacement of the trough base by ~12 longitude ($12 \times 111\,\text{km} \times \cos(17.5°) \approx 1270\,\text{km}$; Fig. 1d). Conversely, in 2000–2020, high-TPS years correspond to positive vorticity anomalies at trough base but negative anomalies downstream, indicating a strengthening of the trough over the Bay of Bengal (Fig. 1e).

Physical processes of TPS impacts on IBT variations

As the "Asian Water Tower"[31–33], the Tibetan Plateau snow drives regional and global climate anomalies via albedo feedback[21,26,34,35] and hydrological effects[20,36,37]. During 1979–1999, a positive-phase TPS index corresponds to a quasi-seesaw snow pattern, which is defined as positive snow anomalies over the central-eastern Tibet versus negative anomalies in the west (Supplementary Fig. 4a). Due to snow-albedo effect, this spatial pattern induces surface to mid-upper atmospheric cooling anomalies (−0.9 to −0.1 K) over the central-eastern regions, contrasting with western warming anomalies (0.2–0.6 K; Supplementary Fig. 4c). Conversely, during 2000–2020, a positive-phase TPS index exhibits a coherent snow pattern, which is defined as widespread positive snow anomalies across the entire Plateau (Supplementary Fig. 4b), driving consistent cooling anomalies from surface through mid-upper atmosphere (−1.1 to −0.2 K; Supplementary Fig. 4d).

Given the interaction between snowpack and atmospheric circulation[38–43], we conduct four sets of snow-perturbation experiments to diagnose circulation responses to different TPS forcings (see "Methods"). During 1979-1999, observations and experiments reveal that the quasi-seesaw TPS pattern drives an upper-tropospheric cyclonic anomaly east of the Tibet and an anticyclone anomaly west of the Tibet (Fig. 2a and Supplementary Fig. 5a). This occurs as the enhanced central-eastern snowpack induces adiabatic cooling, whereas the western reduced snow cover promotes adiabatic heating (Supplementary Fig. 4c). In contrast, during 2000-2020, the coherent TPS pattern generates a broad upper-tropospheric cyclone anomaly across the Tibet (Fig. 2b) via a uniform adiabatic cooling (Supplementary Fig. 4d).

During 1979–1999, the positive quasi-seesaw TPS pattern triggers a lower tropospheric anticyclone-cyclone-anticyclone circulation anomaly

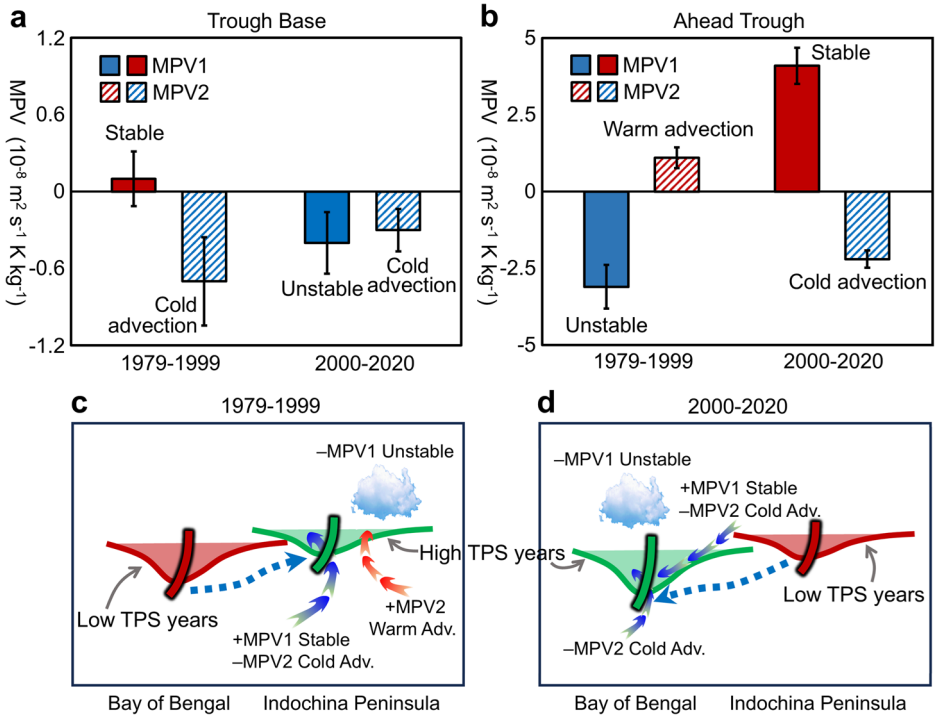

Fig. 3 | Theoretical diagnostics of TPS-driven IBT dynamics. Spring moisture potential vorticity (MPV1/MPV2, 1PVU = 10^{-6} m^2 s^{-1} K kg^{-1}) anomalies at 700 hPa for **a** trough base and **b** ahead of trough regions, shown as area-mean differences between high and low TPS years during 1979–1999 and 2000–2020. Physically, MPV1 > 0: Convectively stability; MPV1 < 0: Convectively instability; MPV2 > 0: Warm advection; MPV2 < 0: Cold advection (see "Methods"). Error bars: 95% CI (confidence intervals; ±1.96 × standard error). Spatial distributions of MPV1 and MPV2 are shown in Supplementary Fig. 7. The schematic (MPV framework) illustrates the reversal in TPS-IBT relationship for **c** 1979–1999 and **d** 2000–2020. Data sources: ERA5 reanalysis datasets.

along the southern Tibet (Fig. 2c). Southwesterly anomalies along the northwestern flank of the western Pacific anticyclonic anomaly (Fig. 2e) enhance climatological southwesterlies (Supplementary Fig. 1b), accelerating background flow and hence promoting trough-ahead development. In addition, these southwesterly anomalies also transport warm advection ahead of the trough (Supplementary Fig. 6a), causing air expansion and lower-tropospheric convergence motions via air mass compensation. As low-level convergence facilitates potential vorticity generation[44,45], positive vorticity anomalies develop ahead of the trough (Fig. 1d). Concurrently, the trough base features southerly and cold anomalies (Fig. 2e). Cold advection (Supplementary Fig. 6a) drives divergent motions, weakening the trough base through potential vorticity dissipation. Collectively, trough-ahead development, base weakening, and the 104°E cold/warm advection boundary (Supplementary Fig. 6a) drive an ~12° eastward displacement of trough base (Fig. 1d).

During 2000-2020, the positive coherent TPS pattern triggers a lower-tropospheric cyclonic anomaly south of the Tibet alongside an eastern anticyclonic anomaly (Fig. 2b). Northeasterly anomalies along this anticyclone opposite climatological southwesterlies, weakening airflow ahead of the trough. These northeasterly anomalies also drive cold advection ahead of the trough (Fig. 2f and Supplementary Fig. 6b). This process leads to potential vorticity dissipation, which reduces trough-ahead intensity. Simultaneously, the cyclonic anomaly (Fig. 2d) strengthens the trough base through potential vorticity generation, deepening the IBT over the Bay of Bengal.

MPV perspective on IBT variation

Based on the physical linkages between IBT variations and TPS forcing, we employ a moist potential vorticity (MPV) framework (see "Methods") to quantify the underlying mechanisms[46–48]. MPV is decomposed into its vertical component (MPV1) and horizontal component (MPV2), where MPV1 < 0 diagnoses convective instability, while MPV1 > 0 indicates stability; MPV2 > 0 signifies warm advection, while MPV2 < 0 denotes cold advection.

During 1979-1999, the positive quasi-seesaw TPS pattern promotes warm advection ahead of the trough (MPV2 = $(1.1 \pm 0.3) \times 10^{-2}$ PVU; Fig. 3b and Supplementary Fig. 7), accompanied by convective instability (MPV1 = $(-3.1 \pm 0.7) \times 10^{-2}$ PVU; Fig. 3b) and positive precipitation anomalies (Supplementary Fig. 6c). The precipitation associated latent heat release from mid-level (600–400 hPa) creates a vertical thermal contrast with lower levels that generates potential vorticity[44,45,49], thereby enhancing positive vorticity anomalies ahead of the trough (Fig. 1d). Conversely, cold advection dominates the trough base (MPV2 = $(-0.7 \pm 0.3) \times 10^{-2}$ PVU; Fig. 3a) with enhanced stability (MPV1 = $(0.1 \pm 0.2) \times 10^{-2}$ PVU; Fig. 3a) and precipitation suppression (Supplementary Fig. 6c), resulting in potential vorticity dissipation. Consequently, this combination of amplified trough-ahead development and suppressed base conditions drives an eastward shift of the trough line (Fig. 3c).

During 2000–2020, the positive coherent TPS pattern induces cold advection ahead of the trough (MPV2 = $(-2.2 \pm 0.3) \times 10^{-2}$ PVU; Fig. 3b and Supplementary Fig. 7), accompanied by enhanced stability (MPV1 = $(4.1 \pm 0.6) \times 10^{-2}$ PVU; Fig. 3b) and precipitation suppression (Supplementary Fig. 6d), resulting in potential vorticity dissipation and consequent trough-ahead weakening (Fig. 1e). At the trough base, cold advection (MPV2 = $(-0.4 \pm 0.2) \times 10^{-2}$ PVU; Fig. 3a) promotes potential vorticity dissipation, while convective instability (MPV1 = $(-0.7 \pm 0.3) \times 10^{-2}$ PVU; Fig. 3a) and positive precipitation anomalies (Supplementary Fig. 6d) enhance potential vorticity generation. As instability exceeds cold advection by ~75%, net trough base deepening occurs. Therefore, suppressed trough-ahead alongside amplified trough base deepening sustains persistent IBT intensification over the Bay of Bengal (Fig. 1e). Overall, the MPV analysis confirms that warm advection and instability ahead of the trough favor IBT eastward shifts before 2000, while opposite conditions enhance IBT deepening after 2000.

Potential role of PDO in modulating relationship reversal

We identify a reversal in interannual IBT-TPS linkage, shifting from negative correlation (1979–1999) to positive (2000–2020). This 21-year transition motivate us to figure out decadal-scale modulations within climate system. Our analysis shows that spring TPS correlates with a positive PDO pattern during 1979–1999, but shift to a negative PDO pattern during 2000–2020, with this signature traceable back to the preceding winter (Supplementary Fig. 8). Notably, the PDO itself undergoes a phase shift around 2000 (Fig. 4a). When the PDO is in positive phase, the IBT-TPS

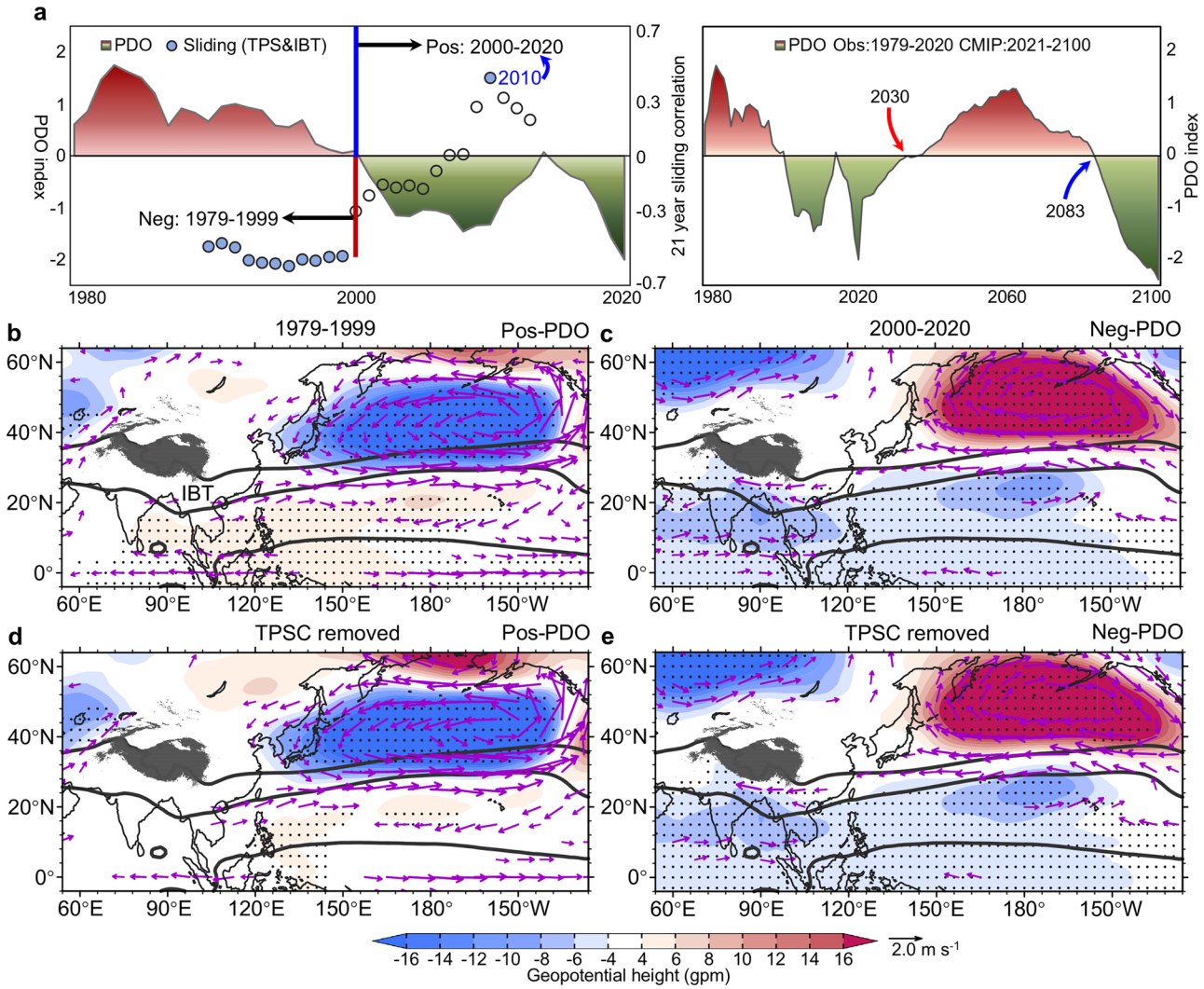

Fig. 4 | PDO modulation of TPS-IBT interannual linkage. a Left panel displays the spring standardized PDO index (10-year running mean based on centered years; color curve) along with 21-year sliding TPS-IBT index correlations (dots). Solid dots indicate correlations significant at the 90% confidence level, whereas open dots represent non-significant correlations. The right panel shows the PDO index from 1979 to 2100, constructed by combing NCAR data (1979–2020) with CMIP5 projections (2021-2100)[71,72]. **b**, **c** Regression patterns 700 hPa geopotential height and wind anomalies against the positive (+PDO; **b**) and negative (-PDO; **c**) phases of the PDO index during 1979-1999 and 2000-2020, respectively. **d**, **e** As in (**b**, **c**), but for partial regression patterns after removing the influence of TPS. Black dots and purple vectors: 95% significant regions (two-tailed *t*-test). Black contours: IBT control zone (700 hPa climatology: 3030/3081.5 gpm). Data sources: NOAA satellite snow cover, ERA5 circulation fields, NCAR PDO index, and CMIP5 PDO index[71,72]. The original data for the CMIP5 PDO index were obtained from refs. 71,72 (under a Creative Commons Attribution-NonCommercial-NoDerivatives 4.0 International License).

correlation is negative, whereas during negative PDO phase, the correlation becomes positive (left panel in Fig. 4a), implying PDO modulates this relationship reversal.

The positive PDO phase (1979-1999; Fig. 4b) is characterized by negative height anomalies over the high-latitudinal North Pacific, but positive height and anticyclone anomalies spanning the tropical northern Indian and Pacific Oceans. The southwesterly anomalies along the northwestern flank of anticyclone resemble those associated with high-TPS patterns (Fig. 1b), suggesting a potential role in promoting eastward displacement of the IBT. Conversely, the negative PDO phase (2000–2020) exhibits markedly contrasting circulation patterns (Fig. 4c). The Bay of Bengal cyclonic circulation corresponds closely to high-TPS conditions (Fig. 1c), enhancing trough base intensification.

After removing the influence of TPS through partial regression, the PDO-driven circulation anomalies over the northern Indian and northwestern Pacific Oceans are clearly weakened (Fig. 4d, e). Over the Bay of Bengal (84°E–105°E, 8°N-22°N), the regression coefficient of the PDO index onto the height field decreases by ~36.1% (from 3.6 gpm to 2.3 gpm) during 1979–1999 and by ~4.3% (from 7.0 gpm to 6.7 gpm) during 2000–2020 after the TPS is accounted for. This result, together with the fact that spring TPS forcing alone can generate similar atmospheric circulation pattern across these regions (Fig. 2), indicates that the TPS acts as a memory mechanism. It stores PDO signals and releases them during spring through snow-induced diabatic forcing, thereby altering the locations of the IBT.

Discussions

Winter IBT variations are linked to local cyclonic anomalies and regulated by mid-latitude teleconnections from tropical forcing[10,15,18,50]. In contrast, this work investigates the origins of spring IBT variability using TPS as a physical driver. The contribution of snow-albedo feedback to elevation-dependent warming on the Tibetan Plateau[51–53] place our findings within the wider context of cryosphere-atmosphere interactions across the Himalaya-Tibetan region.

Variations in the IBT position directly affect precipitation distribution, highlighting its implication for future drought and flood risks. Under the negative phase of the PDO (since 2000), the TPS-associated IBT has

strengthened over the Bay of Bengal, enhancing spring rainfall across South (~0.6–0.8 mm/day) and Southeast Asia (~0.9–1.2 mm/day; Supplementary Fig. 6d). This increase in precipitation likely led to a higher incidence of extreme hydrological events, exemplified by the markedly increased risk of severe flash floods and geological hazards in western India since 2000[54]. A notable recent example is the catastrophic 2022 Pakistan floods, the event that may have been influenced by anomalous TPS conditions during the preceding spring[55]. Multi-model projections from 21 representative CMIP5 models indicate that the negative PDO phase is expected to persist until the early 2030 s (right panel in Fig. 4a), suggesting that these elevated flood risks are projected to persist through 2030.

During the positive PDO phase, the TPS-associated IBT moves eastward, which enhances precipitation in the East Asian monsoon region while reduces rainfall over the Indochina Peninsula due to heightened geopotential heights (Supplementary Figs. 5c, 6d). Given the recurrent spring droughts in these areas[56,57], this reduction in rainfall significantly exacerbates the risk of drought. Multi-model simulations indicate that from the 2030 s to the 2080 s, the PDO is expected to transition to a positive phase (right panel in Fig. 4a), thereby intensifying drought risks across these regions.

Although previous studies identify winter TPS as a precursor to regional climate anomalies[30,58,59], our analysis shows that the IBT-linked TPS signal originates from TPS increment during the preceding winter half-year —not winter TPS (Supplementary Fig. 9). This distinction likely stems from the stronger adiabatic cooling produced by Tibetan Plateau snow accumulation versus snow cover extent[26], making winter half-year snow accumulation a key predictor for spring IBT forecasts.

Notably, although numerical modeling confirms TPS modulates IBT dynamics (Fig. 2), the IBT (or Bay of Bengal cyclonic circulation) also influences Tibetan Plateau precipitation[2,60–62]. In addition, this study reveals that the PDO modulates TPS-IBT linkage, but the reversal in the TPS-IBT relationship occurs around 2000, 1 year prior to the PDO phase shift in 2001. This implies that TPS-IBT reversal may affect the subsequent phase transition of the PDO. These complex interactions necessitate further investigation to disentangle their causality, which is crucial for advancing mechanistic understanding of the TPS-IBT linkages.

Methods

Satellite observations and reanalysis datasets

Three snow datasets were used: satellite-derived weekly snow cover extent obtained from the National Oceanic and Atmospheric Administration (NOAA, spanning 1979–2023)[63] and the National Snow and Ice Data Center (NSIDC, covering 1979–2020)[64], and model-based ERA5-Land snow depth data sourced from the fifth generation of ECMWF's atmospheric reanalysis (ERA5, covering 1979–2023)[65].

Notably, the central-eastern Tibetan Plateau (89°E–103°E, 26°N–36°N) exhibits extensive spring snow cover with high interannual variability[25,66]. To characterize this variability, we defined the spring TPS index as the area-weighted mean of snow cover across this region. Index values were detrended, subjected to interannual filtering and standardized. All datasets produced TPS indices with coherent fluctuations (Supplementary Fig. 10), showing stronger inter-dataset correlation: 0.96 (NOAA/NSIDC) and 0.53 (NOAA/ERA5-Land; all $p < 0.001$), confirming robust interannual variability capture.

Atmospheric variables including wind, vorticity, temperature, geopotential height, specific humidity, and precipitation fields (1950–2023) were derived from ERA5 reanalysis[67]. For verification, we additionally employed the National Centers for Environmental Prediction–Department of Energy Reanalysis-2 (NCEP-R2, covering 1979-2024;)[68] datasets, yielding consistent findings. Monthly global sea surface temperature data (1870–2024) were obtained from the HadISST dataset provided by the UK Met Office Hadley Centre[69].

The PDO is defined as the leading Empirical Orthogonal Function of North Pacific sea surface temperature anomalies, according to Mantua et al.[70]. The historical PDO index (1854–2024) was sourced from the National Center for Atmospheric Research (NCAR). Future projections of the PDO index were derived from previous studies[71,72], which employed 21 representative models from the Coupled Model Intercomparison Project Phase 5 (CMIP5). Using statistical synthesis and spatiotemporal correlation methods, these studies produced a PDO time series for the 21st century. This projected series has been calibrated against observational data to ensure consistency in phase transitions with the historical record.

Tibetan Plateau snow forcing experiments

While conventional snow-forcing experiments simulate snow effcts via proxies, such as albedo modifications, diabatic cooling, or atmospheric divergence[27,66,73,74], we directly force models with satellite-observed snow cover anomalies to integrate snow-albedo and hydrological feedbacks. This approach establishes a more direct physical linkages between TPS forcing and atmospheric responses. We implement this scheme using the NCAR Community Earth System Model version 1.2 Large Ensemble (CESM-LEN)[75]. The CESM-LEN configuration couples CAM4 (the Community Atmosphere Model v4) with CLM4.5 (the Community Land Model v4.5), incorporating ocean and sea-ice components.

Four snow perturbation experiments were performed using satellite-derived TPS anomalies (see Supplementary Table 2 for details). (1) Positive quasi-seesaw TPS experiment (Pos^{SS}_{Exp}): Forced with positive-phase TPS anomalies (Supplementary Fig. 4a). (2) Negative quasi-seesaw TPS experiment (Neg^{SS}_{Exp}): Forced with negative-phase TPS anomalies. Each experiment comprised 45 ensemble members. Observational TPS anomalies were imposed over the Tibetan Plateau to drive CESM-LEN, and climatological sea surface temperatures and sea-ice were prescribed to isolate snow-forced responses. After discarding the initial 25 years as model spin-up, the final 20 ensemble members were analyzed. Atmospheric responses to the quasi-seesaw TPS forcing were assessed by calculating the ensemble mean difference ($Pos^{SS}_{Exp} - Neg^{SS}_{Exp}$) to isolate the TPS forcing impacts (Fig. 2a, c, e).

Following the quasi-seesaw experiments, we conducted additional two coherent TPS forcing experiments. (3) Positive coherent TPS experiment (Pos^{CHR}_{Exp}): Forced with positive-phase TPS anomalies (Supplementary Fig. 4b). (4) Negative coherent TPS experiment (Neg^{CHR}_{Exp}): Forced with negative-phase anomalies. All experimental configurations remained identical to the quasi-seesaw experiments: 45-member ensembles, prescribed sea surface temperature and sea-ice concentrations, and analysis of the final 20 equilibrated members. Atmospheric responses were quantified as the ensemble mean difference ($Pos^{CHR}_{Exp} - Neg^{CHR}_{Exp}$; Fig. 2b, d, f).

MPV diagnosis of TPS impacts on IBT dynamics

Moist potential vorticity (MPV) theory extends the dry Ertel potential vorticity framework to capture diabatic and baroclinic processes in moist air masses[45,76]. This approach quantitatively diagnoses vertical vorticity generation, tropical stroms, squall lines, and precipitation dynamics[46,47,77]. Validated for phase-changing moist atmospheres, we employ MPV theory to quantify IBT dynamical development and movement (Fig. 3). Following established formulations[46,47,76], MPV is defined as:

$$MPV = -g\left(\zeta_p + f\right)\frac{\partial\theta_{se}}{\partial p} + g\left(\frac{\partial v}{\partial p}\frac{\partial\theta_{se}}{\partial x} - \frac{\partial u}{\partial p}\frac{\partial\theta_{se}}{\partial y}\right) \quad (1)$$

$$MPV1 = -g\left(\zeta_p + f\right)\frac{\partial\theta_{se}}{\partial p} \quad (2)$$

$$MPV2 = g\left(\frac{\partial v}{\partial p}\frac{\partial\theta_{se}}{\partial x} - \frac{\partial u}{\partial p}\frac{\partial\theta_{se}}{\partial y}\right) \quad (3)$$

where ζ_p denotes relative vorticity, g gravity acceleration, f the Coriolis parameter, and θ_{se} equivalent potential temperature, with u and v representing zonal and meridional wind fields, respectively.

MPV1 diagnoses convective instability: positive values indicate atmospheric stability, while negative values denote convective instability. MPV2 quantifies moist baroclinicity; positive values signify warm advection

whereas negative values indicate cold advection. Since both baroclinicity and convective instability enhance the generation of vertical vorticity[46–48], the configuration MPV1 < 0 and MPV2 > 0 fosters optimal conditions for trough development.

Definition of the IBT indices

During boreal spring, the IBT trough base lies over the Bay of Bengal, exhibiting its maximum variability over the region 84°–105°E, 8°–22°N (Supplementary Fig. 1a). Adopting the winter IBT index methodology based on 700 hPa vorticity field[2,13,15], we define the spring IBT index as the area-weighted mean 700 hPa vorticity field over this domain. Unlike winter IBT variability confined primarily to the northern Bay of Begnal[2,10], the spring trough extends eastward into the western Pacific (Supplementary Fig. 1a, inset), reflecting enhanced zonal mobility (Fig. 1d, e). To better characterize this zonal displacement, we introduce a height-based IBT index: the area-weighted mean 700 hPa geopotential height over 84°–105°E, 8°–22°N.

We employ both the vorticity-based and height-based IBT indices to investigate their interannual connections with TPS. Sliding correlation analysis using both indices produces consistent results (Fig. 1a). Sensitivity tests with 19-year and 21-year moving windows confirm robust transition timing in this relationship, indicating a statistically significant regime shift in TPS-IBT linkage.

Statistical analysis

To investigate the physical mechanisms through which TPS influence IBT variations, we identified high- and low-TPS years using ±0.5 standard deviation thresholds (Supplementary Table 1). Composite analyses of atmospheric fields were conducted for these selected years. Statistical significance was evaluated using a two-sided *t*-test, with composite *t* statistics for high- and low-TPS years calculated as:

$$t = \frac{\overline{\frac{1}{N_H}\sum_i x_i} - \overline{\frac{1}{N_L}\sum_j x_j}}{s_p\sqrt{\frac{1}{N_H}+\frac{1}{N_L}}} \tag{4}$$

$$s_p = \sqrt{\frac{(N_H-1)s_H^2 + (N_L-1)s_L^2}{N_H + N_L - 2}} \tag{5}$$

where N_H and N_L denote the sample sizes for high- and low-TPS years, respectively. s_H and s_L represent sample standard deviation for high- and low-TPS years, respectively. s_p indicates the standard deviation across both groups. The degree of freedom is estimated through:

$$N_{df} = \frac{\left(\frac{s_H^2}{N_H}+\frac{s_L^2}{N_L}\right)^2}{\left\{\left[\frac{(s_H^2/N_H)^2}{N_H-1}\right]+\left[\frac{(s_L^2/N_L)^2}{N_L-1}\right]\right\}} \tag{6}$$

We employed partial regression analysis to examine how the PDO modulates TPS's independent influence on IBT variability. This method statistically isolates PDO's dynamical role by removing TPS-covarying components through:

$$\alpha(x,y) = \sum_{t=1}^{m}\left(\mathrm{PDO}'_{\mathrm{res}}(t)\cdot Y'_{\mathrm{res}}(x,y,t)\right) / \sum_{t=1}^{m}\left(\mathrm{PDO}'_{\mathrm{res}}(t)^2\right) \tag{7}$$

where α is the partial regression coefficient quantifying PDO's independence influence, and Y denotes the target atmospheric circulation fields. The regression residuals are calculated as: $\mathrm{PDO}_{\mathrm{res}}(t) = \mathrm{PDO}(t) - \beta_{\mathrm{TPS}\to\mathrm{PDO}} \times \mathrm{TPS}\ (t)$; $Y_{\mathrm{res}}(x, y, t) = Y(x, y, t) - \beta_{\mathrm{TPS}\to\mathrm{PDO}} \times \mathrm{TPS}\ (t)$. Primed terms (e.g., PDO′) denote deviations from the temporal mean.

To isolate the interannual TPS-IBT linkage, we applied a high-pass Butterworth filter with a cutoff frequency of 0.125 year^{-1} to both indices and spatial fields. This filter removes climate variability on timescale longer than 8 years, retaining sub-8-year interannual fluctuation. Additionally, linear least squares quantified coverability between TPS indices (Supplementary Fig. 10). Statistical significance of the composite and regression analysis was assessed using the two-sided Student's *t*-test, with $p < 0.1$ and $p < 0.05$ defining the 90% and 95% confidence levels, respectively.

Data availability

The figures and indices used in this study are available on Zenodo[78] at https://doi.org/10.5281/zenodo.17120424; The NSIDC snow cover data are available at: https://doi.org/10.5067/P7O0HGJLYUQU; The NOAA snow cover data are available at: https://doi.org/10.7289/V5N014G9; The ERA5-Land snow depth are available at: https://doi.org/10.24381/cds.68d2bb30; The ERA5 atmospheric variables at: https://doi.org/10.24381/cds.6860a573; The Met Office Hadley Centre sea surface temperature are available at: https://www.metoffice.gov.uk/hadobs/hadisst/; The NCEP-R2 atmospheric variables are available at: https://doi.org/10.5065/FPR3-MW53; The NCAR PDO index are available at: https://climatedataguide.ucar.edu/climate-data/pacific-decadal-oscillation-pdo-definition-and-indices; The future PDO index is available at https://github.com/atrmli/data.

Code availability

The composite and partial regression analysis were performed using scripts developed with the Intel® Fortran Compiler, which is publicly available on Zenodo[79] at https://doi.org/10.5281/zenodo.17117540. Other codes are available upon request from the corresponding author.

Received: 28 September 2025; Accepted: 10 December 2025;
Published online: 26 December 2025

References

1. Yin, M. T. Synoptic-aerologic study of the onset of the summer monsoon over India and Burma. *J. Atmos. Sci.* **6**, 393–400 (1949).
2. Li, X. & Zhou, W. Modulation of the interannual variation of the India-Burma Trough on the winter moisture supply over Southwest China. *Clim. Dyn.* **46**, 147–158 (2016).
3. Suo, M. & Ding, Y. The structures and evolutions of the wintertime southern branch trough in the subtropical westerlies. *Chin. J. Atmos. Sci.* **33**, 425–442 (2009).
4. Chan, J. C., Shi, J.-e. & Lam, C.-m. Seasonal forecasting of tropical cyclone activity over theWestern North Pacific and the South China Sea. *Wea. Forecast.* **13**, 997–1004 (1998).
5. Wang, T., Yang, S., Wen, Z., Wu, R. & Zhao, P. Variations of the winter India-Burma Trough and their links to climate anomalies over southern and eastern Asia. *J. Geophys. Res. Atmos.* **116**, D23118 (2011).
6. Lü, J., Ju, J., Ren, J. & Gan, W. The influence of the Madden-Julian Oscillation activity anomalies on Yunnan's extreme drought of 2009–2010. *Sci. China Earth Sci.* **55**, 98–112 (2012).
7. Wang, Y., Ren, F., Zhao, Y. & Li, Y. Comparison of two drought indices in studying regional meteorological drought events in China. *J. Meteorol. Res.* **31**, 187–195 (2017).
8. Zhou, W. et al. Synoptic-scale controls of persistent low temperature and icy weather over southern China in January 2008. *Mon. Weather Rev.* **137**, 3978–3991 (2009).
9. Wang, M. & Li, X. The joint influences of the South Asian Jet Wave Train and Eurasian Teleconnection on the wet–cold extreme over South China in February 2022. *J. Clim.* **37**, 6235–6252 (2024).
10. Lu, B. & Ren, H.-L. SST-forced interdecadal deepening of the winter India-Burma trough since the 1950s. *J. Geophys. Res. Atmos.* **121**, 2719–2731 (2016).
11. Singh, V. K., Roxy, M. K. & Deshpande, M. Role of subtropical Rossby waves in governing the track of cyclones in the Bay of Bengal. *Q. J. Roy. Meteor. Soc.* **148**, 3774–3787 (2022).
12. Huang, S., Li, X. & Wen, Z. Characteristics and possible sources of the intraseasonal South Asian jet wave train in boreal winter. *J. Clim.* **33**, 10523–10537 (2020).

13. Li, X., Chen, Y. D. & Zhou, W. Response of winter moisture circulation to the India–Burma trough and its modulation by the South Asian waveguide. *J. Clim.* **30**, 1197–1210 (2017).
14. Yin, J. et al. Role of the subtropical westerly jet wave train in the eastward-moving heavy rainfall event over southern China in winter: a case study. *Front. Earth Sci.* **11**, 1107674 (2023).
15. Li, X., Wen, Z. & Zhou, W. Different configurations of the Eurasian pattern and South Asian jet wave train and their impacts on the winter climate over East Asia. *Clim. Dyn.* **62**, 5787–5806 (2024).
16. Bhardwaj, P., Pattanaik, D. R. & Singh, O. Tropical cyclone activity over Bay of Bengal in relation to El Niño-Southern Oscillation. *Int. J. Climatol.* **39**, 5452–5469 (2019).
17. Liu, K., Li, H., Zhou, L.-T., Wang, Z. & Liu, Y. An interdecadal shift of India–Burma trough in spring around 2000 and its possible reason. *Atmos. Oceanic Sci. Lett*. 100689 (2025).
18. Rong, Y., Zhang, L. & Wu, F. An investigation of heat source effect of Tibetan Plateau on the wintertime India-Burma Trough. *Glob. Planet. Change* **192**, 103222 (2020).
19. Nan, S. & Zhao, P. Snowfall over central-eastern China and Asian atmospheric cold source in January. *Int. J. Climatol.* **32**, 888–899 (2012).
20. Kraaijenbrink, P., Stigter, E., Yao, T. & Immerzeel, W. W. Climate change decisive for Asia's snow meltwater supply. *Nat. Clim. Chang.* **11**, 1–7 (2021).
21. Zhang, C., Jia, X. & Wen, Z. Increased impact of the Tibetan Plateau spring snow cover to the Mei-yu rainfall over the Yangtze River valley after the 1990s. *J. Clim.* **34**, 5985–5997 (2021).
22. Jin, Y., Liu, Z. & Duan, W. The different relationships between ENSO spring persistence barrier and predictability barrier. *J. Clim.* **35**, 1–28 (2022).
23. Zhao, S. et al. Explainable El Niño predictability from climate mode interactions. *Nature* **630**, 891–898 (2024).
24. Levine, A. F. & McPhaden, M. J. The annual cycle in ENSO growth rate as a cause of the spring predictability barrier. *Geophys. Res. Lett.* **42**, 5034–5041 (2015).
25. Zhang, C., Guo, Y. & Wen, Z. Interdecadal change in the effect of Tibetan Plateau snow cover on spring precipitation over Eastern China around the early 1990s. *Clim. Dyn.* **58**, 2807–2824 (2022).
26. Zhang, C., Duan, A., Jia, X., Wang, Z. & Pan, Z. A dynamic link between spring Arctic sea ice and the Tibetan Plateau snow increment indicator. *npj Clim. Atmos. Sci.* **6**, 191 (2023).
27. Zhang, C., Duan, A., Jia, X., Hu, J. & Liu, S. Snow Cover on the Tibetan Plateau and Lake Baikal Intensifies the Winter North Atlantic Oscillation. *Geophys. Res. Lett.* **50**, e2023GL104754 (2023).
28. Huang, J. et al. Global climate impacts of land-surface and atmospheric processes over the Tibetan Plateau. *Rev. Geophys.* **61**, e2022RG000771 (2023).
29. Li, W. et al. Influence of Tibetan Plateau snow cover on East Asian atmospheric circulation at medium-range time scales. *Nat. Commun.* **9**, 4243 (2018).
30. Si, D. & Ding, Y. Decadal change in the correlation pattern between the Tibetan Plateau winter snow and the East Asian summer precipitation during 1979-2011. *J. Clim.* **26**, 7622–7634 (2013).
31. Zhang, F., Zeng, C., Zhang, Q. & Yao, T. Securing water quality of the Asian Water Tower. *Nat. Rev. Earth Env.* **3**, 611–612 (2022).
32. Yao, T. et al. The imbalance of the Asian water tower. *Nat. Rev. Earth Env.* **3**, 1–15 (2022).
33. Immerzeel, W. et al. Importance and vulnerability of the world's water towers. *Nature* **577**, 364–369 (2020).
34. Jia, X., Zhang, C., Wu, R. & Qian, Q. Influence of Tibetan Plateau autumn snow cover on interannual variations in spring precipitation over southern China. *Clim. Dyn.* **56**, 767–782 (2021).
35. Qian, Q., Jia, X. & Wu, R. Changes in the impact of the autumn Tibetan Plateau snow cover on the winter temperature over North America in the mid-1990s. *J. Geophys. Res. Atmos.* **124**, 10321–10343 (2019).
36. Kapnick, S. B., Delworth, T. L., Ashfaq, M., Malyshev, S. & Milly, P. C. D. Snowfall less sensitive to warming in Karakoram than in Himalayas due to a unique seasonal cycle. *Nat. Geosci.* **7**, 834–840 (2014).
37. Smith, T. & Bookhagen, B. Changes in seasonal snow water equivalent distribution in High Mountain Asia (1987 to 2009). *Sci. Adv.* **4**, e1701550 (2018).
38. Man, K. et al. Century-long West Antarctic snow accumulation changes induced by tropical teleconnections. *Sci. Adv.* **11**, eadr2821 (2025).
39. Gottlieb, A. R. & Mankin, J. S. Evidence of human influence on Northern Hemisphere snow loss. *Nature* **625**, 293–300 (2024).
40. Preece, J. R. et al. Summer atmospheric circulation over Greenland in response to Arctic amplification and diminished spring snow cover. *Nat. Commun.* **14**, 3759 (2023).
41. Zhang, H., Zhang, F., Zhang, G. & Yan, W. Why Do CMIP6 models fail to simulate snow depth in terms of temporal change and high mountain snow of China skillfully?. *Geophys. Res. Lett.* **49**, e2022GL098888 (2022).
42. Henderson, G., Peings, Y., Furtado, J. & Kushner, P. Snow-atmosphere coupling in the Northern Hemisphere. *Nat. Clim. Chang.* **8**, 954–963 (2018).
43. Cohen, J., Agel, L., Barlow, M., Garfinkel, C. & White, I. Linking Arctic variability and change with extreme winter weather in the United States. *Science* **373**, 1116–1121 (2021).
44. Wu, G., Ma, T., Liu, Y. & Jiang, Z. PV-Q perspective of cyclogenesis and vertical velocity development downstream of the Tibetan Plateau. *J. Geophys. Res. Atmos.* **125**, e2019JD030912 (2020).
45. Hoskins, B. J., McIntyre, M. E. & Robertson, A. W. On the use and significance of isentropic potential vorticity maps. *Q. J. Roy. Meteor. Soc.* **111**, 877–946 (1985).
46. Zhang, F., Pu, Z. & Wang, C. Land-surface diurnal effects on the asymmetric structures of a postlandfall tropical storm. *J. Geophys. Res. Atmos.* **126**, 2020JD033842 (2021).
47. Xu, C., Qiao, Y. & Jian, M. Interdecadal change in the intensity of interannual variation of spring precipitation over Southern China and possible reasons. *J. Clim.* **32**, 5865–5881 (2019).
48. Wu, G.-X. & Liu, H.-Z. Vertical vorticity development owing to down-sliding at slantwise isentropic surface. *Dynam. Atmos. Oceans* **27**, 715–743 (1998).
49. Li, J. et al. Development mechanisms of cyclonic vorticity under two distinct large-scale weather patterns associated with summer heavy rainfall over North China. *Clim. Dyn.* **62**, 10579–10597 (2024).
50. Lin, X., Lu, B., Li, G., Gao, C. & Chen, L. Asymmetric impacts of El Niño–Southern Oscillation on the winter precipitation over South China: the role of the India–Burma Trough. *Clim. Dyn.* **61**, 2211–2227 (2023).
51. Guo, D., Yu, E. & Wang, H. Will the Tibetan Plateau warming depend on elevation in the future?. *J. Geophys. Res. Atmos.* **121**, 3969–3978 (2016).
52. Guo, D., Pepin, N., Yang, K., Sun, J. & Li, D. Local changes in snow depth dominate the evolving pattern of elevation-dependent warming on the Tibetan Plateau. *Sci. Bull.* **66**, 1146–1150 (2021).
53. Rangwala, I., Miller, J. R. & Xu, M. Warming in the Tibetan Plateau: possible influences of the changes in surface water vapor. *Geophys. Res. Lett.* **36**, L06703 (2009).
54. Dilip K., N., Vegad, U. & Mishra, V. Drivers of flash floods in the Indian sub-continental river basins. *npj Nat. Hazards*. **2**, 62 (2025).
55. Ma, Q. et al. Impact of spring Tibetan Plateau snow cover on extreme precipitation in Pakistan in July and August 2022. *Atmos. Res.* **295**, 107007 (2023).
56. Chhin, R., Oeurng, C. & Yoden, S. Drought projection in the Indochina Region based on the optimal ensemble subset of CMIP5 models. *Clim. Chang.* **162**, 687–705 (2020).
57. Gao, Q.-G., Sombutmounvong, V., Xiong, L., Lee, J.-H. & Kim, J.-S. Analysis of drought-sensitive areas and evolution patterns through statistical simulations of the Indian Ocean dipole mode. *Water* **11**, 1302 (2019).

58. Xu, X. et al. Downstream effect" of winter snow cover over the eastern Tibetan Plateau on climate anomalies in East Asia. *J. Meteorol. Soc. Jpn.* **90C**, 113–130 (2012).
59. Wu, T.-W. & Qian, Z.-A. The relation between the Tibetan winter snow and the Asian summer monsoon and rainfall: an observational investigation. *J. Clim.* **16**, 2038–2051 (2003).
60. He, L., Zhou, T. & Guo, Z. Past warm intervals inform the future South Asian summer monsoon. *Nature* **641**, 653–659 (2025).
61. Jiang, J. et al. Precipitation regime changes in High Mountain Asia driven by cleaner air. *Nature* **623**, 544–549 (2023).
62. Kad, P. & Ha, K.-J. Recent tangible natural variability of monsoonal orographic rainfall in the Eastern Himalayas. *J. Geophys. Res. Atmos.* **128**, e2023JD038759 (2023).
63. Robinson, D. A., Estilow, T. W. & Program, N. C. NOAA Climate Data Record (CDR) of Northern Hemisphere (NH) Snow Cover Extent (SCE), Version 1 [NCDC: C00756]. NOAA National Centers for Environmental Information. Accessed 17 June 2024 (2012).
64. Brodzik, M. J. & Armstrong, R. Northern Hemisphere EASE-Grid 2.0 Weekly Snow Cover and Sea Ice Extent, Version 4 [NSIDC-0046]. Boulder, Colorado USA. NASA National Snow and Ice Data Center Distributed Active Archive Center. Accessed 1 July 2023 (2013).
65. Muñoz Sabater, J. ERA5-Land monthly averaged data from 1950 to present. *Copernicus Climate Change Service (C3S) Climate Data Store (CDS)*. Accessed 09 July 2024 (2019).
66. Wang, Z., Wu, R., Duan, A. & Qu, X. Influence of eastern Tibetan Plateau spring snow cover on North American air temperature and its interdecadal change. *J. Clim.* **33**, 5123–5139 (2020).
67. Hersbach, H. et al. ERA5 monthly averaged data on single levels from 1940 to present. *Copernicus Climate Change Service (C3S) Climate Data Store (CDS),* Accessed 09 July 2024 (2023).
68. Kanamitsu, M. et al. NCEP-DOE AMIP-II Reanalysis (R-2). *Bull. Am. Meteorol. Soc.* **83**, 1631–1643 (2002).
69. Rayner, N. A. et al. Global analyses of sea surface temperature, sea ice, and night marine air temperature since the late Nineteenth Century. *J. Geophys. Res.* **108**, 4407 (2003).
70. Mantua, N. J. & Hare, S. R. The Pacific decadal oscillation. *J. Oceanogr.* **58**, 35–44 (2002).
71. Zhang, Q. et al. Climate impacts and future trends of hailstorms in China based on millennial records. *Nat. Commun.* **16**, 8000 (2025).
72. Wu, H., Yan, P., Hou, W., Zhao, J. & Feng, G. Detection of decadal phase transition and early warning signals of PDO in recent and next 100 years. *Chin. J. Atmos. Sci.* **46**, 225–236 (2022).
73. Zhang, C. & Jia, X. The seasonal evolution of the Tibetan Plateau snow cover related moisture during spring-to-summer. *J. Geophys. Res. Atmos.* **127**, e2022JD036560 (2022).
74. Wang, C., Yang, K., Li, Y., Wu, D. & Bo, Y. Impacts of spatiotemporal anomalies of Tibetan Plateau snow cover on summer precipitation in Eastern China. *J. Clim.* **30**, 885–903 (2017).
75. Kay, J. E. et al. The Community Earth System Model (CESM) large ensemble project: a community resource for studying climate change in the presence of internal climate variability. *Bull. Am. Meteorol. Soc.* **96**, 1333–1349 (2015).
76. Wu, G., Cai, Y. & Tang, X. Moist potential vorticity and slantwise vorticity development. *Acta Meteor. Sin.* **53**, 387–404 (1995).
77. Zhang, D.-L. & Cho, H.-R. The development of negative moist potential vorticity in the stratiform region of a simulated squall line. *Mon. Weather Rev.* **120**, 1322–1341 (1992).
78. Zhang, C. Datasets used in the study "Reversal of the Tibetan snow-India Burma trough relationship" [Data set]. Zenodo. https://doi.org/10.5281/zenodo.17120424 (2025).
79. Zhang, C. Fortran codes used in the study "Reversal of the Tibetan snow-India Burma trough relationship" (version 1.0). Zenodo. https://doi.org/10.5281/zenodo.17117540 (2025).

Acknowledgements

C.Z. acknowledges financial support from the Outstanding Postdoctoral Scholarship provided by the State Key Laboratory of Marine Environmental Science at Xiamen University and the Chinese Scholarship Council (File No.202306310194). This research was supported by the National Natural Science Foundation of China through grants 42305016 (to C.Z.) and 42030602 (to A.D.), and the Joint Funds of the National Natural Science Foundation of China through grants U2442205 (to A.D.).

Author contributions

C.Z. conceived the study, conducted simulations and wrote the initial manuscript. All authors performed the formal analysis. A.D provided critical feedback and revised the manuscript.

Competing interests

The authors declare no competing interests.

Additional information

Supplementary information The online version contains supplementary material available at https://doi.org/10.1038/s41612-025-01301-8.

Correspondence and requests for materials should be addressed to Chao Zhang or Anmin Duan.